Letter

Nadir-Dependent GNSS Code Biases and their Effect on 2D and 3D Ionosphere Modeling

Martin Håkansson [1,2]

[1] Lantmäteriet—The Swedish Mapping, Cadastral, and Land Registration Authority, S-801 82 Gävle, Sweden; martin.hakansson@lm.se

[2] Division of Geodesy and Satellite Positioning, KTH Royal Institute of Technology, Teknikringen 10 B, S-100 44 Stockholm, Sweden

Abstract: Recent publications have shown that group delay variations are present in the code observables of the BeiDou system, as well as to a lesser degree in the code observables of the global positioning system (GPS). These variations could potentially affect precise point positioning, integer ambiguity resolution by the Hatch–Melbourne–Wübbena linear combination, and total electron content estimation for ionosphere modeling from global navigation satellite system (GNSS) observations. The latter is an important characteristic of the ionosphere and a prerequisite in some applications of precise positioning. By analyzing the residuals from total electron content estimation, the existence of group delay variations was confirmed by a method independent of the methods previously used. It also provides knowledge of the effects of group delay variations on ionosphere modeling. These biases were confirmed both for two-dimensional ionosphere modeling by the thin shell model, as well as for three-dimensional ionosphere modeling using tomographic inversion. BeiDou group delay variations were prominent and consistent in the residuals for both the two-dimensional and three-dimensional case of ionosphere modeling, while GPS group delay variations were smaller and could not be confirmed due to the accuracy limitations of the ionospheric models. Group delay variations were, to a larger extent, absorbed by the ionospheric model when three-dimensional ionospheric tomography was performed in comparison with two-dimensional modeling.

Keywords: GNSS; group delay variations; biases; nadir dependence; ionosphere modeling; ionospheric tomography

1. Introduction

Signals in the frequency bands employed by global navigation satellite systems (GNSSs) are affected by the ions and free electrons in the part of the atmosphere referred to as the ionosphere [1]. As the ionosphere is dispersive, GNSSs have been designed to employ multiple carrier frequencies. This allows almost complete elimination of the effect from GNSS code and phase observations. Conversely, availability of observations associated with multiple carrier frequencies also allow for determination of the number of free electrons and ions in the ionosphere by forming the geometry-free linear combination [1].

By utilization of the geometry-free linear combination of GNSS observations, the total electron content (TEC) along the ray paths can be estimated. Doing this for several satellites and several receivers allows for estimation of the spatial distribution of TEC. A two-dimensional (2D) vertical TEC (VTEC) distribution can be estimated and distributed as a global ionospheric map (GIM) where the modelling is based on the "thin shell" model and a mapping function between slant ionospheric delays and vertical delays [1]. A more complete three-dimensional (3D) model might be derived by computerized ionospheric tomography (CIT) [2–4], techniques that were inspired by and have emerged from computerized tomography (CT) for medical applications [5].

GNSS hardware biases [6], and especially biases in the code observations, are well-known to affect the estimation of TEC from GNSS observations [7–9]. These biases, referred to as differential code biases (DCBs), are regarded as constant offsets between code observations associated with two signals transmitted between the same satellite and receiver. Thereby, an offset exists in addition to the expected offset due to different ionospheric influence caused by the difference in carrier frequencies. However, even though these biases have been assumed to be constant, recent findings by Hauschild et al. [10], Wanninger and Beer [11], and Wanninger et al. [12] show that the code biases also have a nadir-dependent component, with the largest effects shown for BeiDou [11], but with measurable effects also shown for other GNSSs [12]. These varying biases of the code observables are also referred to as group delay variations (GDV).

Previous studies by Wanninger and Beer [11] and Wanninger, Sumaya, and Beer [12] have shown that nadir-dependent GDV affect precise point positioning (PPP) based on the single frequency ionosphere-free combination, wide-lane ambiguity fixing based on the Hatch–Melbourne–Wübbena linear combination [13–15], as well as TEC estimation of the ionosphere. The latter is an important characteristic of the ionosphere and is necessary in some single frequency precise positioning applications, for instance, precise positioning with mobile devices, which has gained significant attention in recent years [16–27]. For the verification and further understanding of these effects, the independent evaluation of previously used methods is therefore important.

In this study, we investigated how nadir-dependent GDV affect ionosphere modeling by analyzing the model residuals that they give rise to. Additionally, this approach demonstrates an alternative way of proving the existence of such biases. Earlier studies have employed the multipath (MP) linear combination [10–12], while, in this study, we derived the corresponding relationships from ionosphere modeling, and more specifically, the geometry-free linear combination of GNSS observations. This study thereby presents a method independent of the previously employed methods for the determination of the nadir dependence of GDV.

The ionosphere modeling was performed regionally over an area covering Sweden with GNSS observations from SWEPOS, the national network of continuously operating reference stations (CORS) in Sweden [28].

2. Methods

The following sections provide a summary of the methods utilized in this work for 2D and 3D ionosphere modeling, as well as for independent derivation of nadir-dependent biases from the MP linear combination.

2.1 Derivation of STECs from GNSS Measurements

GNSS signals are affected by free electrons in the ionosphere during their transmission between satellite and receiver. Slant total electron content (STEC) is given by

$$STEC = \int N_e ds \tag{1}$$

where N_e is the ionospheric electron density (IED) along the ray path of the GNSS signal. STEC is a measure of the total effect of free-charged particles of the ionosphere on the GNSS signal. It is related to the GNSS observables as a delay for code observations and an advance for carrier phase measurements. The size of the effect is dependent on the carrier frequency for the frequency bands employed. This enables either isolation or elimination of the ionospheric effect by linearly combining GNSS observations associated with several carrier frequencies. Isolation of the first-order term can be achieved by the geometry-free linear combination of code or phase observations associated with two carrier frequencies [7] through

$$R_{1,r}^s - R_{2,r}^s = (1-\gamma)I_{1,r}^s + DCB_{21,r} - DCB_{21}^s + M_{1,r}^s - M_{2,r}^s + \varepsilon_{R21,r}^s \tag{2}$$

$$L_{2,r}^s - L_{1,r}^2 = (1-\gamma)I_{1,r}^s + B_{12,r}^s + m_{2,r}^s - m_{1,r}^s + \varepsilon_{L21,r}^2 \tag{3}$$

where

$$\gamma = \frac{f_1^2}{f_2^2} \tag{4}$$

and

$$B_{12,r}^s = \left(b_{2,r} - b_2^s\right) - \left(b_{1,r} - b_1^s\right) + N_{2,r}^s - N_{1,r}^s \tag{5}$$

In these equations, a quantity $(\cdot)_{f,r}^s$ is associated with carrier frequency *f*, receiver *r*, and satellite *s*; *R* is a code observable; *L* is a phase observable (in units of length); *I* is the ionospheric influence; *DCB* is the differential code bias (DCB) that is due to code biases caused by both the receiver and the satellite hardware; *M* is code multipath; *B* is combined receiver, b_r, and satellite phase biases, b^s, lumped together with the phase ambiguities, *N*; *m* is phase multipath; and ε is noise and other unhandled errors.

In this study, STECs were estimated considering only the first-order ionospheric term, derived with Equations (2), (3), and (6). This is acceptable, as the higher-order terms only amount to one centimeter at most [29], which is well below the expected accuracy for ionosphere modeling.

Considering only the first-order term, the TEC is related to ionospheric influence for code and phase observations by

$$I = \frac{40.3}{f^2} TEC \tag{6}$$

where *I* is the ionospheric influence from Equation (2) and (3), and *f* is the carrier frequency [30].

Before the derivation of STECs, the DCBs were calibrated for each receiver with a GIM from the International GNSS Service (IGS) [31] over a period of 24 hours. One receiver DCB for each of the reference stations and one satellite DCB for each of the satellites were estimated by least-squares adjustment in accordance with Equation (2). Multipath and noise were assumed to average out over the 24-hour observation period. For this calibration, the DCBs were considered as constant over time. Possible nadir dependence of code biases will thereby show up in the later stage as residuals from the ionosphere modeling. To avoid the complexity in handling additional GLONASS related biases, only GNSS observations from GPS, Galileo, and BeiDou were employed in the subsequent analysis. For BeiDou, only observations from BeiDou-2 satellites were available at the time of this study.

2.2 Ionosphere Modeling in 2D

One common way to model the ionosphere is by an assumption that all the electron content of the ionosphere is distributed over an infinitely thin layer in the so-called "thin shell" model. The height of the shell is preferably chosen to the height of the largest concentration level of free-charged particles. STECs that refer to the slant signal path are in this model converted to vertical TEC (VTEC). This is done with the ionospheric mapping function for a thin shell [1]

$$F(z) = \frac{1}{\cos z} \tag{7}$$

where $STEC = F(z)VTEC$ and *z* is the zenith angle at the ionospheric pierce point (IPP), which is the intersection between the GNSS signal path and the thin shell. STECs derived from GNSS measurements are thereby mapped as VTECs on the IPPs. In the next step, a 2D model of the VTEC distribution over the shell is created with a spherical harmonics expansion of the VTECs on the IPPs. The spherical harmonics expansion is achieved through

$$VTEC(\phi,\lambda) = \sum_{n=0}^{n_{max}} \sum_{m=0}^{n} \tilde{P}_{nm}(\sin\phi)\left(\tilde{C}_{nm}\cos(m\lambda) + \tilde{S}_{nm}\sin(m\lambda)\right) \tag{8}$$

where ϕ is the latitude, λ is the longitude, $\tilde{P}_{nm}$ is the normalized associated Legendre function of degree *n* and order *m*, $\tilde{C}_{nm}$ and $\tilde{S}_{nm}$ are spherical harmonics coefficients to be determined. Equation (8) is a slightly modified version of the one found in Schaer [1]. In this study, a geographic longitude was used instead of sun-fixed longitude, as each observation epoch was handled independently and no interpolation was done between epochs.

2.3 Computerized Iionospheric Tomography (CIT)

The 3D TEC distribution can be estimated with tomographic inversion. For an inversion volume defined regionally, this is often done by representing the ionospheric electron density (IED) distribution over a finite number of voxels, i.e., volume elements, with constant IED in each voxel. This can be represented as a linear observation model expressed in vector form as

$$\mathbf{l}_{M \times 1} = \mathbf{A}_{M \times N} \mathbf{x}_{N \times 1} \tag{9}$$

where $\mathbf{l}$ is a vector with M STEC observations along the ray paths, $\mathbf{x}$ is the vector of IEDs for each of the N voxels, and $\mathbf{A}$ is a matrix with distances that the signal travels through each of the voxels. The problem of finding the IEDs in $\mathbf{x}$ is typically ill-posed for a network of receivers placed on the ground, and a unique least-squares solution to Equation (9) is therefore generally not possible to find.

Several strategies that address this issue have been developed over the years. These strategies can be divided into iterative and noniterative inversion methods. The basic iterative methods include the algebraic reconstruction technique (ART) [4] and the multiplicative algebraic reconstruction technique (MART) [32]. Improvements of these, as well as new methods, have been suggested and applied in ionospheric tomography, for instance, the simultaneous iteration reconstruction technique (SIRT) [33], the decomposed algebraic reconstruction technique (DART) [2], and the improved algebraic reconstruction technique (IART) [34].

Noniterative inversion methods, including for instance singular value decomposition (SVD) [35] and truncated singular value decomposition (TSVD) [36], are worth mentioning as well. These methods achieve solutions in a least-squares-least-norm sense and share similarities with Tikhonov regularization. Generally, an ill-posed and unsolvable problem might be regularized to a solvable problem by adding additional cost terms to the objective function. In the case of Tikhonov regularization, an objective to minimize the norm is added to the problem formulation. In other noniterative inversion methods ,regularization is demonstrated by adding smoothness objectives, minimizing the difference of IEDs between adjacent voxels [37–39].

Successful tomographic inversion is dependent on the geometric distribution of the observations available. Figure 1 depicts the average number of signals that travelled through each voxel for an inversion volume defined over Sweden where observations from the three GNSSs GPS, Galileo, and BeiDou were employed. As can be observed, voxels on high latitudes and high altitudes generally suffer by a lower availability of GNSS observations. The relatively low availability of observations on higher latitudes means that the tomographic inversion will be more challenging than for regions close to the equator with more favorable GNSS satellite geometries.
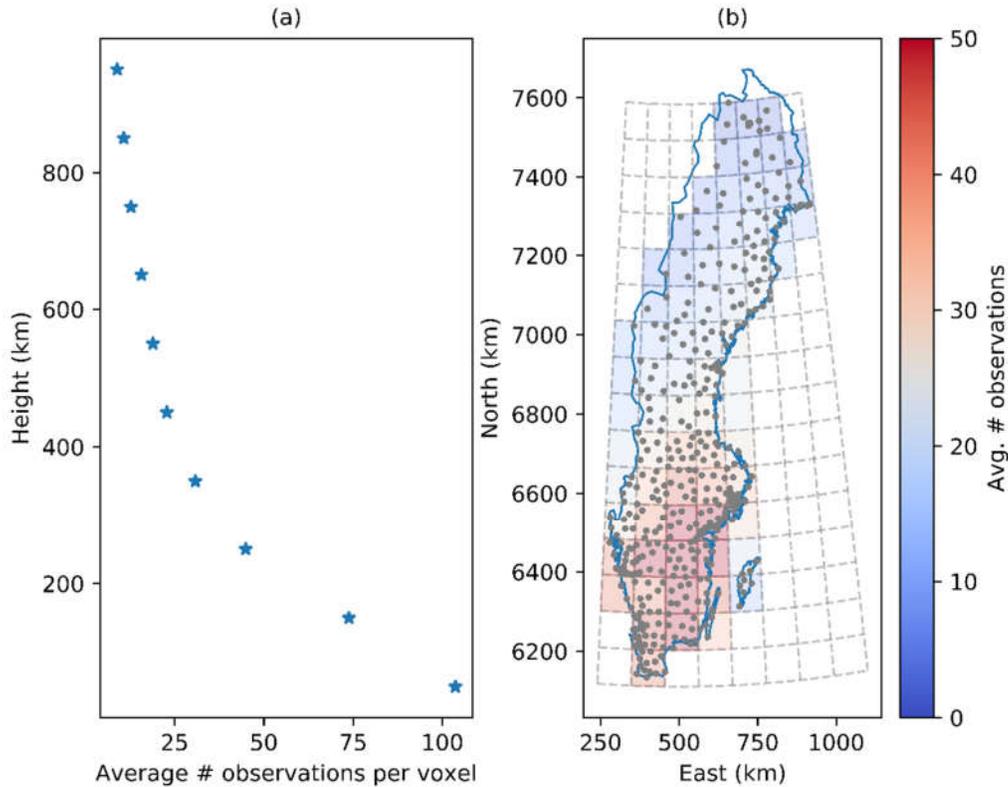
Figure 1. Average number of (#) observations per voxel for ionospheric tomography versus altitude (**a**) and geographic location (**b**).

To achieve optimal usage of the available GNSS measurements, side rays were also utilized in this study. Side rays are rays that partially pass through the ionosphere outside of the inversion volume. As they therefore only partially coincide with the inversion volume, they are traditionally not employed in ionospheric tomography, since the part of the STEC originating for the inversion volume is unknown. According to the method described by Yao et al. [40], partial STECs (PSTECs) can be determined for the side rays by

$$PSTEC = STEC_{GNSS} \times \frac{PSTEC_{NeQuick2}}{STEC_{NeQuick2}} \tag{10}$$

where $STEC_{GNSS}$ are the total STECs determined from GNSS measurements by Equation (2) and (3). $PSTEC_{NeQuick2}$ and $STEC_{NeQuick2}$ are determined from the deterministic three-dimensional ionosphere electron density model NeQuick2 [41].

Even though additional information might be incorporated into the tomographic inversion by regularization, it is not possible to include inequality constraints with the closed form least squares adjustment formulas derived from the normal equations. One drawback is thus that, even with regularization, the solutions produced by such approaches might still, for instance, include negative IEDs.

In this study, we imposed smoothness and constrained the solution to only positive IEDs by applying convex optimization. This optimization technique finds the optimal value of a convex objective function that is constrained over a convex set of possible solutions. Optimality of the final

solution is guaranteed by strong duality, which applies generally for convex optimization problems [42].

With this method, the inversion was done by solving the convex optimization problem

$$\underset{x \in \mathbb{R}^n}{\text{minimize}} \quad \|\mathbf{Bx}\|_1$$

$$\text{subject to} \quad \|\mathbf{Ax} - \mathbf{l}\|_2 \leq \sigma \cdot \sqrt{M}$$
$$\mathbf{Dx} \geq \mathbf{0}$$
$$\mathbf{Cx} = \mathbf{0}$$
$$\mathbf{x} \geq \mathbf{0}$$

where $\|\cdot\|_1$ and $\|\cdot\|_2$ are the L1 and L2 norms, respectively. $\mathbf{B}$ is a matrix for estimation of differences between adjacent voxels belonging to the same layer, i.e., for the row vector $\mathbf{B}_i$ in $\mathbf{B}$

$$\mathbf{B}_i \mathbf{x} = \mathbf{x}_{j1} - \mathbf{x}_{j2} \tag{12}$$

for two adjacent voxels $\mathbf{x}_{j1}$ and $\mathbf{x}_{j2}$ belonging to the same layer. The $\mathbf{D}$ matrix ensures that the top side electron density profile decreases at least at a certain rate. For the row vector $\mathbf{D}_i$ in $\mathbf{D}$

$$\mathbf{D}_i \mathbf{x} = \tfrac{1}{2}\mathbf{x}_{h1} - \mathbf{x}_{h2} \tag{13}$$

where voxel $\mathbf{x}_{h2}$ lies directly above $\mathbf{x}_{h1}$. This constraint is only active above 350 km and prevents unreasonably large IED values for high altitudes. The $\mathbf{C}$ matrix identifies voxels in the top and bottom layer, and thus according to the problem, the formulation sets these to zero.

The convexity of Equation (11) follows from convexity of the L1 and L2 norms together with the convexity of linear constraints [42]. This inversion method was inspired by methods employing regularization achieving smoothness by adding the total variation (TV) norm as a cost term to the objective function [38,43]. A slightly simplified approach is to minimize the L1 norm of differences between adjacent voxels instead. Like with the TV norm, some edge preservation is achieved as minimization of the L1 norm tends to produce sparse solutions. This approach is beneficial, as the problem can be solved with a convex solver. In this study, this was done in Julia [44] with the embedded conic solver (ECOS) [45]. The suggested inversion method described in Equation (11) was evaluated against the NeQuick 2 model and some of the previously mentioned inversion methods, including ART, MART, SIRT, SVD, and regularization with minimization of IED differences between adjacent voxels. It proved to be superior regarding the challenging satellite geometries for the high latitudes involved in this study.

2.4 Alternative Method to Determine Nadir-Dependent Biases

The existence of nadir-dependent GDV was demonstrated in the investigation of signal anomalies associated with the GPS SVN 49 satellite [46]. Later studies also proved the existence of prominent nadir-dependent GDV of BeiDou second generation medium Earth orbiting (MEO) and inclined geosynchronous orbiting (IGSO) satellites [11]. Less prominent nadir-dependent GDV have also been demonstrated to exist for GPS observations [12].

Earlier methods have proved the existence of GDV by employing the MP linear combination of GNSS observations. By forming this combination, it is possible to isolate variations of a selected code observable, given that dual frequency carrier phase observations are available from the same satellite. The MP linear combination is formed by

$$MP_{f_1,r}^s = P_{f_1,r}^s + (\eta_{f_1 f_2} - 1)L_{f_1} - \eta_{f_1 f_2} L_{f_2} - B \tag{14}$$

where

$$\eta_{f_1 f_2} = \frac{2\lambda_{f_1}^2}{\lambda_{f_1}^2 - \lambda_{f_2}^2} \qquad (15)$$

where *P* is a code observation, *L* is a phase observation in units of length, λ is the carrier wavelength, and *B* is phase ambiguities lumped together with hardware code and phase biases [29].

To separate the nadir-dependent part of the GDV from noise and local multipath, a spherical harmonics expansion of degree 5 and order 0 was used as regression model. This regression model for determination of nadir-dependent GDV was demonstrated by the authors of [12]. With this technique, high-frequency variations, probably consisting of noise and local high-frequency multipath, are filtered away, while low-frequency variations persist.

2.5 Data Processing

In this study, data processing was done according to the flowchart presented in Figure 2. First, DCBs were calibrated with GNSS observations from SWEPOS reference stations and a GIM from the IGS. This was done with Equation (2), as described in Montenbruck and Hauschild [47], with data covering a period of 24 hours. An elevation mask of 15 degrees was applied for the GNSS observation data. In the next step, STECs were estimated from calibrated DCBs and reference station GNSS observation data with Equations (2) and (3). This was done from the GNSS observations of about 400 SWEPOS reference stations, which are distributed over Sweden with a maximum distance between stations of 70 km. The estimated STECs were used as observations in both 2D and 3D ionosphere modeling as described by Equations (8) and (11). In the later analysis, residuals from the ionosphere modeling were compared with GDV derived from the MP linear combination described in Equation (14).
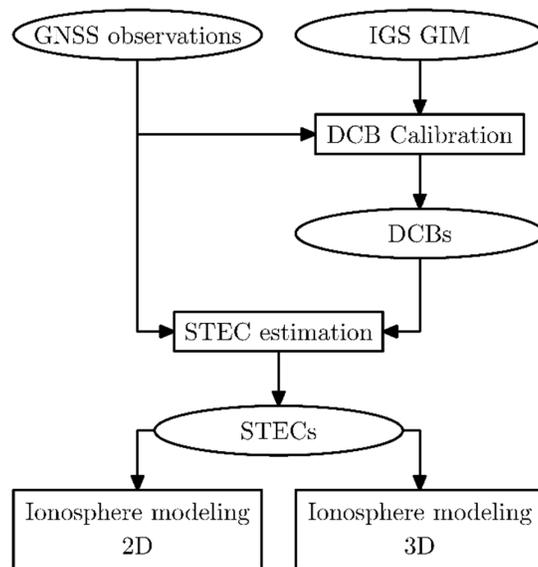

Figure 2. Flowchart of the data processing steps.

2.6 Handling of Remaining Error Sources

Local code multipath is a considerable error source that is not cancelled when forming the geometry-free linear combination. To mitigate this error source without removing the long-term

variations of the code observable, the estimated code STECs were fitted to carrier phase STECs over 15-minute intervals. Of the fitted STECs, only the middle epoch in each interval was used in the subsequent ionosphere modeling. By doing this, a considerable part of the TEC estimation errors due to multipath and code noise were removed. Multipath and code noise amounted to a few decimeters at the SWEPOS sites, which might have employed choke ring antennas, and were located at places with favorable multipath conditions. After the fitting of code STECs to carrier phase STECS, all data processing was performed independently between epochs. This approach was chosen to avoid introducing extra time dependencies in the end results due to assumptions of the dynamics made by the estimation method.

Error sources with contributions of only a few centimeters were ignored in the data processing because uncertainties at this level did not affect the ionosphere modeling performed in this study, as the modeling errors themselves amounted to the decimeter level. The error sources ignored included phase wind-up [48], which only amounted to a few centimeters, and phase center offsets at the reference stations and at the satellites. For phase center offsets, only the relative offsets associated with different carrier frequencies remained for the geometry-free linear combination. As only variations over the nadir and elevation angle intervals were of interest in this study, this, in practice, also only amounted to a few centimeters. For the receiver antennas, the relative phase center offsets for the Dorne-Margolin antennas used within SWEPOS were a few centimeters, which was negligible. At the satellite side, a nadir angle interval of 0-14 degrees amounts to a variation of only 0.03 times the phase center offset [12]. In the case of the geometry-free linear combination, the relative phase center offsets were assumed to be at the meter level, which meant an effect of a few centimeters for the small nadir angle interval.

3. Results

Ionosphere modeling was performed in two and three dimensions from using three days of GNSS observation data, day of year (DOY) 180–182 in 2018. This is a period almost free from ionospheric disturbances, which means that the smoothness assumed in Equations (8) and (11) was more likely to be valid. STECs were estimated from the geometry-free linear combination according to Equations (2) and (3) from the GNSS signal combinations C1C-C2W, C6X-C1X, and C1X-C5X for GPS, BeiDou, and Galileo, respectively with signals denoted in accordance with the receiver independent exchange format RINEX 3 [49]. The residuals of the ionosphere modeling were analyzed and compared with GDV derived from the MP linear combination. As only regional ionosphere modeling was performed, only some of the satellites were observed over longer nadir angle intervals. It was thereby only possible to analyze the nadir angle dependence for a subset of all satellites belonging to the constellations of GPS, BeiDou, and Galileo.

3.1 Ionosphere Modeling in 2D

A 2D ionosphere model was estimated over Sweden with spherical harmonics expansion by Equation (8) and the assumption that the ionosphere was distributed over an infinitely thin layer according to the "thin shell" model. The height of the layer was set to 450 km, which was the same as for the GIMs used for the DCB calibration. Both the degree and order of the spherical expansion were conservatively set to 20 based on the reference station density of the network.

Figures 3–5 present residuals for a sample of three satellites of 2D ionosphere modeling compared with GDV derived by the MP linear combination for GPS, BeiDou, and Galileo, respectively. Due to the estimation method, with regional ionosphere modeling, only a subset of all satellites could be processed over larger nadir intervals. The satellites with residuals available for the longest nadir angle intervals were selected, but the results are representable also for other visible satellites. In these figures, residuals are marked with blue stars and connected with line segments for a complete satellite pass, which includes angle dependencies both for the satellite rising and for the satellite setting. In these figures, the MP combination values themselves (orange dots), as well as the spherical harmonics expansion regression model values (green line), were shifted to the average level of the residuals. The residuals and the regression model values followed the same trend, especially

for BeiDou-2 satellites, which were also expected to have larger GDV. The sizes of the BeiDou GDV, with a range of about 10 TECU, are in good agreement with previous studies by Hauschild, Montenbruck, Sleewaegen, Huisman, and Teunissen [10] and Wanninger and Beer [11]. For GPS and Galileo, the variations were considerably smaller, and it was thus harder to draw any conclusion as these were at, or below, the expected accuracy of the ionosphere model. The variations that can be observed were at a level that agrees with the findings of Wanninger, Sumaya, and Beer [12], which also confirmed that the GDV are less prominent for GPS. However, the receiver antenna also induced GDV of similar sizes, which could not be separated in the results.
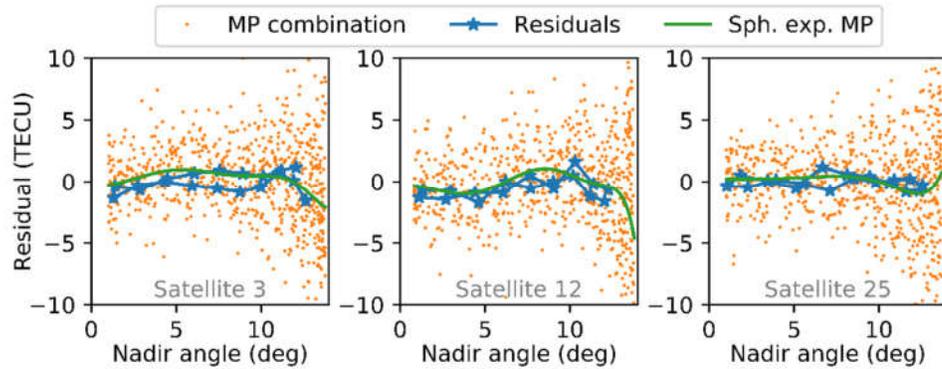
Figure 3. Residuals from two-dimensional (2D) ionosphere modeling compared with nadir-dependent biases derived by the multipath (MP) combination for three global positioning system (GPS) satellites (G03, G12, G25).
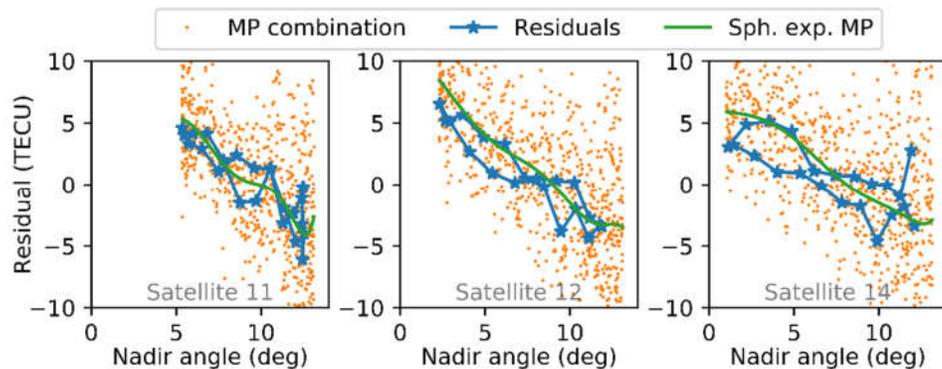
Figure 4. Residuals from 2D ionosphere modeling compared with nadir-dependent biases derived by the MP combination for three BeiDou satellites. (C11, C12, C14).
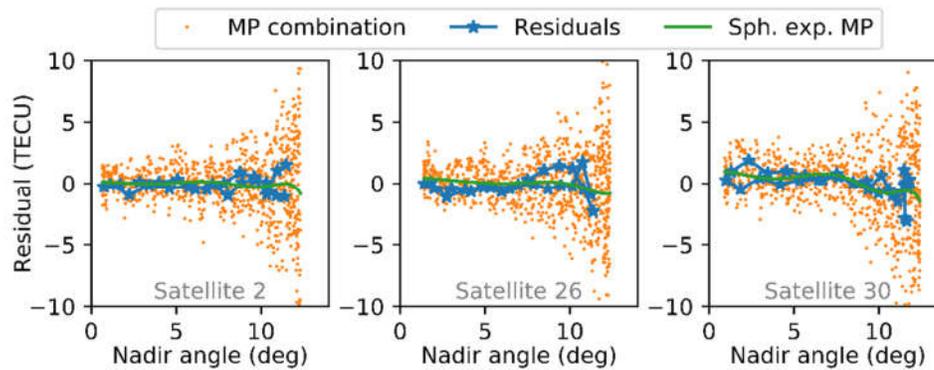
Figure 5. Residuals from 2D ionosphere modeling compared with nadir-dependent biases derived by the MP combination for three Galileo satellites (E02, E26, E30).

3.1 Ionospheric Tomography

Ionospheric tomography with the inversion method described by Equation (11) was utilized to determine a 3D ionospheric model of IEDs over Sweden. The inversion volume with voxels and reference stations is depicted in Figure 1 and included all voxel columns coincident with the colored squares of the figure.

Figures 6–8 present the residuals from ionospheric tomography compared with GDV derived by the MP linear combination. Similar to the 2D case, the GDV for BeiDou, with a range of about 7 TECU, were considerably larger than the GDV for GPS and Galileo, but still not as large as the MP linear combination suggests. This might be an indication that some of the GDV were absorbed by the ionospheric model. The absorption of GDV by the model could be caused by the correlation between the GDV and the model parameters. This was more likely for the tomographic inversion problem, as this model was ill-conditioned and had considerably more degrees of freedom than the model in the 2D case. Similar to the 2D case, the GDV were small for GPS and Galileo, and the values fell below the expected accuracy of the ionosphere model.
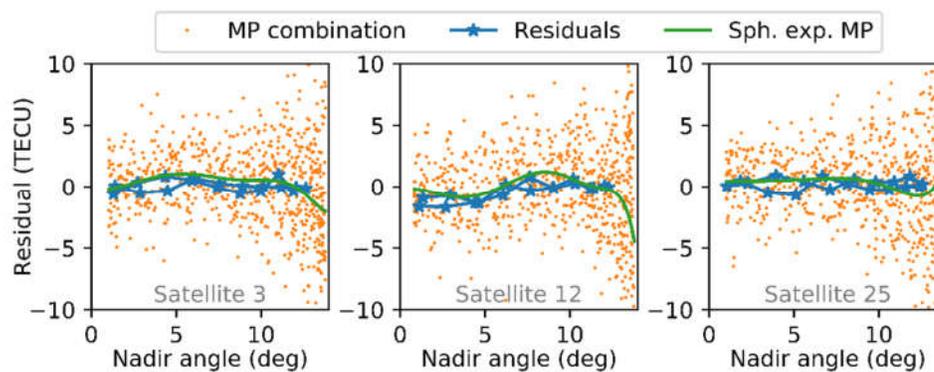

Figure 6. Residuals from three-dimensional (3D) ionospheric tomography modeling compared with nadir-dependent biases derived by the MP combination for three GPS satellites (G03, G12, G25).
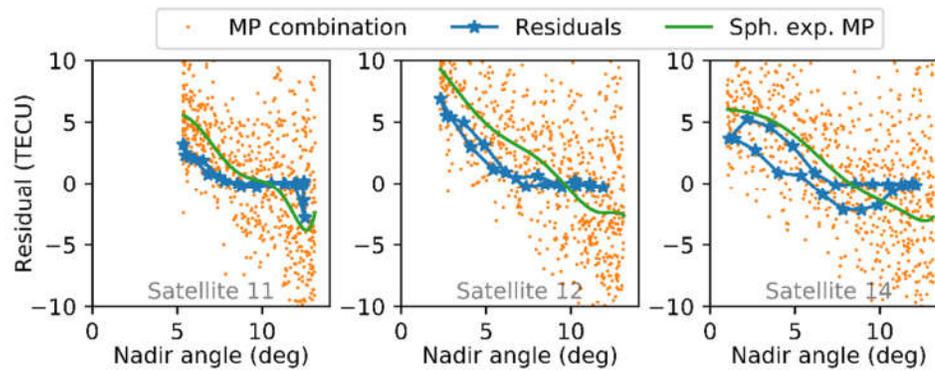
Figure 7. Residuals from 3D ionospheric tomography modeling compared with nadir-dependent biases derived by the MP combination for three BeiDou satellites (C11, C12, C14).
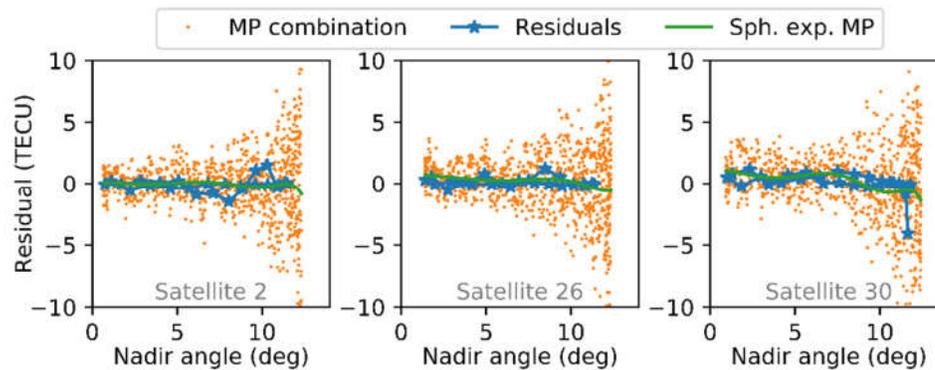

Figure 1. Residuals from 3D ionospheric tomography modeling compared with nadir-dependent biases derived by the MP combination for three Galileo satellites (E02, E26, E30).

4. Discussion

The results show large nadir-dependent GDV for the BeiDou-2 satellite for both 2D and 3D ionosphere modeling, making the results consistent for both types of ionosphere modeling even though they fundamentally differed in the way they modeled the ionosphere. They are also consistent in size with the results of previous studies [10,11]. Furthermore, the shown BeiDou-2 variations of the residuals, of about 10 TECU for 2D ionosphere modeling and about 7 TECU for 3D ionosphere modeling, were too large to be caused by remaining possible error sources, which included TEC estimation errors due to, for instance, low-frequency multipath, modeling errors, unmodeled phase wind-up and phase center offsets, and GDV of the receiver antenna. These error sources did not contribute more than on the decimeter level. Using the same reasoning, nadir-dependent GDV cannot be inferred for GPS and Galileo by analyzing residuals from the two types of ionosphere modeling, as the variations for these systems lie below the expected sizes of remaining not considered error sources.

5. Conclusions

This paper describes developments and testing of a new approach for estimation, as well as a characterization of the nadir-dependent GDV. This is done by analyzing the residuals from ionosphere modeling based on the geometry-free linear combination of GNSS code and phase

observations. The approach was investigated for ionosphere modeling both in 2D, with the "thin shell" model, as well as 3D with tomographic inversion.

Nadir-dependent GDV are known from previous studies to be present in the code observable, especially for BeiDou-2 IGSO and MEO satellites, but also for GPS to a lesser degree. It was verified that these GDV indeed were present and affects both 2D and 3D ionosphere modeling by spherical harmonics expansion of VTECs and ionospheric tomography. Investigating the residuals of ionosphere modeling shows that these effects are especially prominent for BeiDou.

The values of GDV estimated for GPS and Galileo could not be verified due to the limited accuracy of the ionosphere modeling. It was also concluded that these GDV were probably absorbed by the ionospheric model in the 3D case with ionospheric tomography to a greater extent. This might be due to the higher number of degrees of freedom in the tomographic problem formulation, and it suggests that ionospheric tomography is more sensitive to GDV than the simpler 2D VTEC modeling. This result also implies that 2D ionosphere modeling with the "thin shell" model might be better suited for GDV characterization than for 3D ionosphere modeling.

It is important to be able to characterize GDV because, as earlier studies demonstrated, they affect PPP, integer ambiguity resolution by the Hatch–Melbourne–Wübbena linear combination, as well as TEC estimation. The latter is important for various precise positioning applications where the ionospheric influence explicitly must be considered.

References

1. Schaer, S. *Mapping and Predicting the Earth's Ionosphere Using the Global Positioning System*; Institut für Geodäsie und Photagrammetrie, Eidg. Technische Hochschule Zürich, 1999.

2. Kunitsyn, V.E.; Tereshchenko, E.D. *Ionospheric Tomography*, 1st ed.; Springer: Berlin/Heidelberg, Germany, 2003, doi:10.1007/978-3-662-05221-1.

3. Raymund, T.D.; Franke, S.J.; Yeh, K.C. Ionospheric tomography: Its limitations and reconstruction methods. *J. Atmos. Terr. Phys.* **1994**, *56*, 637–657, doi:10.1016/0021-9169(94)90104-X.

4. Austen, J.R. Ionospheric imaging using computerized tomography. *Radio Sci.* **1988**, *23*, 299–307, doi:10.1029/RS023i003p00299.

5. Gordon, R.; Bender, R.; Herman, G.T. Algebraic Reconstruction Techniques (ART) for three-dimensional electron microscopy and X-ray photography. *J. Theor. Biol.* **1970**, *29*, 471–476, doi:10.1016/0022-5193(70)90109-8.

6. Håkansson, M.; Jensen, A.B.O.; Horemuz, M.; Hedling, G. Review of code and phase biases in multi-GNSS positioning. *GPS Solut.* **2017**, *21*, 849–860, doi:10.1007/s10291-016-0572-7.

7. Jensen, A.B.O.; Øvstedal, O.; Grinde, G. Development of a Regional Ionosphere Model for Norway. In Proceedings of the ION GNSS 2007, Fort Worth, TX, USA, 25–28 September 2007; pp. 2880–2889.

8. Lanyi, G.E.; Roth, T. A comparison of mapped and measured total ionospheric electron content using global positioning system and beacon satellite observations. *Radio Sci.* **1988**, *23*, 483–492, doi:10.1029/RS023i004p00483.

9. Sardon, E.; Zarraoa, N. Estimation of total electron content using GPS data: How stable are the differential satellite and receiver instrumental biases? *Radio Sci.* **1997**, *32*, 1899–1910, doi:10.1029/97RS01457.

10. Hauschild, A.; Montenbruck, O.; Sleewaegen, J.-M.; Huisman, L.; Teunissen, P.J.G. Characterization of Compass M-1 signals. *GPS Solut.* **2012**, *16*, 117–126, doi:10.1007/s10291-011-0210-3.

11. Wanninger, L.; Beer, S. BeiDou satellite-induced code pseudorange variations: Diagnosis and therapy. *GPS Solut.* **2015**, *19*, 639–648, doi:10.1007/s10291-014-0423-3.

12. Wanninger, L.; Sumaya, H.; Beer, S. Group delay variations of GPS transmitting and receiving antennas. *J. Geod.* **2017**, *91*, 1099–1116, doi:10.1007/s00190-017-1012-3.

13. Hatch, R. The Synergism of GPS Code and Carrier Measurements. In Proceedings of the Third International Symposium on Satellite Doppler Positioning at Physical Sciences Laboratory of New Mexico State University, Las Cruces, NM, USA, 8–12 February 1982; pp. 1213–1231.

14. Melbourne, W.G. The case for ranging in GPS-based geodetic systems. In Proceedings of the First International Symposium on Precise Positioning with the Global Positioning System, Rockville, MD, USA, 15–19 April 1985; pp. 373–386.

15. Wübbena, G. Software developments of geodetic positioning with GPS using TI 4100 code and carrier measurements. In Proceedings of the First International Symposium on Precise Positioning with the Global Positioning System, Rockville, MD, USA, 15–19 April 1985; pp. 403–412.

16. Håkansson, M. Characterization of GNSS observations from a Nexus 9 Android tablet. *GPS Solut.* **2019**, *23*, doi:10.1007/s10291-018-0818-7.

17. Banville, S.; Van Diggelen, F. Precision GNSS for everyone: Precise Positioning Using Raw GPS Measurements from Android Smartphones. *GPS World* **2016**, *27*, 43–48.

18. Geng, J.; Li, G. On the feasibility of resolving Android GNSS carrier-phase ambiguities. *J. Geod.* **2019**, *93*, 2621–2635, doi:10.1007/s00190-019-01323-0.

19. Gill, M.; Bisnath, S.; Aggrey, J.; Seepersad, G. Precise Point Positioning (PPP) using Low-Cost and Ultra-Low-Cost GNSS Receivers. In Proceedings of the (ION GNSS 2017), Portland, OR, USA, 25–29 September 2017; pp. 226–236.

20. Li, G.; Geng, J. Characteristics of raw multi-GNSS measurement error from Google Android smart devices. *GPS Solut.* **2019**, *23*, doi:10.1007/s10291-019-0885-4.

21. Navarro-Gallardo, M.; Bernhardt, N.; Kirchner, M.; Redenkiewicz Musial, J.; Sunkevic, M. Assessing Galileo Readiness in Android Devices Using Raw Measurements. In Proceedings of the (ION GNSS 2017), Portland, OR, USA, 25–29 September 2017; pp. 85–100.

22. Niu, Z.; Nie, P.; Tao, L.; Sun, J.; Zhu, B. RTK with the Assistence of an IMU-Based Pedestrian Navigation Algorithm for Smartphones. *Sensors* **2019**, *19*, doi:10.3390/s19143228.

23. Paziewski, J.; Sieradzki, R. Signal characterization and assessment of code GNSS positioning with low-power consumption smartphones. *GPS Solut.* **2019**, *23*, doi:10.1007/s10291-019-0892-5.

24. Pirazzi, G.; Mazzoni, A.; Biagi, L.; Crespi, M. Preliminary Performance Analysis with a GPS+Galileo Enabled Chipset Embedded in a Smartphone. In Proceedings of the (ION GNSS 2017), Portland, OR, USA, 25–29 September 2017; pp. 101–115.

25. Realini, E.; Caldera, S.; Pertusini, L.; Sampietro, D. Precise GNSS Positioning Using Smart Devices. *Sensors* **2017**, *17*, doi:10.3390/s17102434.

26. Riley, S.; Lentz, W.; Clare, A. On the Path to Precision - Observations with Android GNSS Observables. In Proceedings of the ION GNSS 2017, Portland, OR, USA, 25–29 September 2017; pp. 116–129.

27. Zhang, X.; Tao, X.; Zhu, F.; Shi, X.; Wang, F. Quality assessment of GNSS observations from an Android N smartphone and positioning performance analysis using time-differenced filtering approach. *GPS Solut.* **2018**, *22*, 70, doi:10.1007/s10291-018-0736-8.

28. Lilje, M.; Wiklund, P.; Hedling, G. The use of GNSS in Sweden and the national CORS network SWEPOS. In Proceedings of the FIG XXV International Congress, Kuala Lumpur, Malaysia, 16–21 June 2014.

29. Leick, A.; Papoport, L.; Tatarnikov, D. *GPS Satellite Surveying*, 4th ed.; John Wiley & Sons, Inc.: Hoboken, NJ, USA, 2015.

30. Hofmann-Wellenhof, B.; Lichtenegger, H.; Wasle, E. *GNSS—Global Navigation Satellite Systems: GPS, GLONASS, Galileo and more*; Springer-Verlag: Wien, Austria, 2008.

31. Dow, J.M.; Neilan, R.E.; Rizos, C. The International GNSS Service in a changing landscape of Global Navigation Satellite Systems. *J. Geod.* **2009**, *83*, 191–198, doi:10.1007/s00190-008-0300-3.

32. Raymund, T.D.; Austen, J.R.; Franke, S.J.; Liu, C.H.; Klobuchar, J.A.; Stalker, J. Application of computerized tomography to the investigation of ionospheric structures. *Radio Sci.* **1990**, *25*, 771–789, doi:10.1029/RS025i005p00771.

33. Pryse, S.E.; Kersley, L.; Rice, D.L.; Russel, C.D.; Walker, I.K. Tomographic imaging of the ionospheric mid-latitude trough. *Ann. Geophys.* **1993**, *11*, 144–149.

34. Wen, D.; Yuan, Y.; Ou, J.; Huo, X.; Zhang, K. Three-dimensional ionospheric tomography by an improved algebraic reconstruction technique. *GPS Solut.* **2007**, *11*, 251–258, doi:10.1007/s10291-007-0055-y.

35. Raymund, T.D.; Bresler, Y.; Anderson, D.N.; Daniell, R.E. Model-assisted ionospheric tomography: A new algorithm. *Radio Sci.* **1994**, *29*, 1493–1512, doi:10.1029/94RS01537.

36. Zhou, C.; Fremouw, E.J.; Sahr, J.D. Optimal trunctation criterion for application of singular value decomposition to ionospheric tomography. *Radio Sci.* **1999**, *34*, 155–166, doi:10.1029/1998RS900015.

37. Lee, J.K. GPS-Based Radio Tomography with Edge-Preserving Regularization. *IEEE Trans. Geosci. Remote Sens.* **2009**, *47*, 312–324, doi:10.1109/TGRS.2008.2001637.

38. Lee, J.K.; Kamalabadi, F.; Makela, J.J. Localized three-dimensional ionospheric tomography with GPS ground receiver measurements. *Radio Sci.* **2007**, *42*, 1–15, doi:10.1029/2006RS003543.

39. Nygrén, T.; Markkanen, M.; Lehtinen, M.; Tereshchenko, E.D.; Khudukon, B.Z. Stochastic inversion in ionospheric radiotomography. *Radio Sci.* **1997**, *32*, 2359–2372, doi:10.1029/97RS02915.

40. Yao, Y.; Zhai, C.; Kong, J.; Zhao, Q.; Zhao, C. A modified three-dimensional ionospheric tomography algorithm with side rays. *GPS Solut.* **2018**, *22*, doi:10.1007/s10291-018-0772-4.

41. Nava, B.; Coïsson, P.; Radicella, S.M. A new version of the NeQuick ionosphere electron density model. *J. Atmos. Sol. Terr. Phys.* **2008**, *70*, 1856–1862, doi:10.1016/j.jastp.2008.01.015.

42. Boyd, S.; Vandenberghe, L. *Convex Optimization*; Cambridge University Press, New York: 2004.

43. Yao, Y.; Tang, J.; Chen, P.; Zhang, S.; Chen, J. An Improved Iterative Algorithm for 3-D Ionospheric Tomography Reconstruction. *IEEE Trans. Geosci. Remote Sens.* **2014**, *52*, 4696–4706, doi:10.1109/TGRS.2013.2283736.

44. Bezanson, J.; Karpinski, S.; Shah, V.B.; Edelman, A. Julia: A Fast Dynamic Language for Technical Computing. *arXiv* **2012**, arXiv:1209.5145.

45. Domahidi, A.; Chu, E.; Boyd, S. ECOS: An SOCP Solver for Embedded Systems. In Proceedings of the European Control Conference (ECC), Zürich, Switzerland, 17–19 July 2013; pp. 3071–3076.

46. Springer, T.; Dilssner, F. SVN49 and Other GPS Anomalies. *Inside GNSS* **2009**, *4*, 32–36.

47. Montenbruck, O.; Hauschild, A. Differential Code Bias Estimation Using Multi-GNSS Observations and Global Ionosphere Maps. In Proceedings of the ITM 2014, San Diego, CA, USA, 27–29 January 2014; pp. 802–812.

48. Wu, J.-T.; Wu, S.C.; Hajj, G.A.; Bertiger, W.I.; Lichten, S.M. Effects of antenna orientation on GPS carrier phase. *Astrodynamics* 1991, **1992**, 1647–1660.

49. IGS; RTCM-SC104. *Rinex—The Receiver Independent Exchange Format—Version 3.02*; Astronomical Institute University of Bern, Switzerland, 2013.